Circulating senescent myeloid cells infiltrate the brain and cause neurodegeneration in histiocytic disorders

C. Matthias Wilk[1,2,3], Flurin Cathomas[4,5,20], Orsolya Török[6,20], Jessica Le Berichel[1,2,3,20], Matthew D. Park[1,2,3,20], Camille Bigenwald[1,2,3,14,15,22], George R. Heaton[7], Pauline Hamon[1,2,3], Leanna Troncoso[1,2,3], Brooks P. Scull[8], Diana Dangoor[9,10,11,12,13], Aymeric Silvin[14,15], Ryan Fleischmann[8], Meriem Belabed[1,2,3], Howard Lin[8], Elias Merad Taouli[1,2,3], Steffen Boettcher[16], Long Li[4,5], Antonio Aubry[4,5], Markus G. Manz[16], Julia K. Kofler[17], Zhenyu Yue[7], Sergio A. Lira[1,2,3], Florent Ginhoux[14,15], John F. Crary[9,10,11,12,13], Kenneth L. McClain[8], Jennifer L. Picarsic[18,19], Scott J. Russo[4,5], Carl E. Allen[8,21,*], Miriam Merad[1,2,3,21,23,*]

[1]Marc and Jennifer Lipschultz Precision Immunology Institute, Icahn School of Medicine at Mount Sinai, New York, NY, USA

[2]The Tisch Cancer Institute, Icahn School of Medicine at Mount Sinai, New York, NY, USA

[3]Department of Oncology Sciences, Icahn School of Medicine at Mount Sinai, New York, NY, USA

[4]Nash Family Department of Neuroscience, Brain & Body Research Center, Friedman Brain Institute, Icahn School of Medicine at Mount Sinai, New York, NY, USA

[5]Friedman Brain Institute, Icahn School of Medicine at Mount Sinai, New York, NY, USA

[6]Department of Neurology, University of Pécs, Medical School, Pécs, Hungary

[7]Department of Neurology and Neuroscience, Friedman Brain Institute, Icahn School of Medicine at Mount Sinai, New York, NY 10029, USA

[8]Texas Children's Cancer Center, Department of Pediatrics, Texas Children's Hospital, Baylor College of Medicine, Houston, TX, USA

[9]Department of Neurology and Neuroscience, Friedman Brain Institute, Icahn School of Medicine at Mount Sinai, New York, NY 10029, USA

*Correspondence: ceallen@texaschildrens.org (C.E.A.), miriam.merad@mssm.edu (M.M.).

[10]Department of Artificial Intelligence, Icahn School of Medicine at Mount Sinai, New York, NY, USA

[11]Nash Family Department of Neuroscience, Icahn School of Medicine at Mount Sinai, New York, NY, USA

[12]Neuropathology Brain Bank and Research CoRE, Icahn School of Medicine at Mount Sinai, New York, NY, USA

[13]Ronald M. Loeb Center for Alzheimer's Disease, Icahn School of Medicine at Mount Sinai, New York, NY, USA

[14]Gustave Roussy Cancer Campus, Villejuif, France

[15]Institut National de la Santé Et de la Recherche Médicale (INSERM) U1015, Equipe Labellisée —Ligue Nationale contre le Cancer, Villejuif, France

[16]Department of Medical Oncology and Hematology, University of Zurich and University Hospital Zurich, Zurich, Switzerland

[17]Division of Neuropathology, Department of Pathology, University of Pittsburgh, Pittsburgh, PA, USA

[18]Division of Pathology, Cincinnati Children's Hospital Medical Center, Cincinnati, OH, USA

[19]Department of Pathology, University of Cincinnati College of Medicine, Cincinnati, OH, USA

[20]These authors contributed equally

[21]These authors contributed equally

[22]Present address: Department of Medicine, Gustave Roussy Cancer Campus, Villejuif, France

[23]Lead contact

SUMMARY

Neurodegenerative diseases (ND) are characterized by progressive loss of neuronal function. Mechanisms of ND pathogenesis are incompletely understood, hampering the development of effective therapies. Langerhans cell histiocytosis (LCH) is an inflammatory neoplastic disorder caused by hematopoietic progenitors expressing mitogen-activated protein kinase (MAPK)-activating mutations that differentiate into senescent myeloid cells that drive lesion formation. Some individuals with LCH subsequently develop progressive and incurable neurodegeneration (LCH-ND). Here, we showed that LCH-ND was caused by myeloid cells that were clonal with peripheral LCH cells. Circulating *BRAF*V600E^{+} myeloid cells caused the breakdown of the blood-brain barrier (BBB), enhancing migration into the brain parenchyma where they differentiated into senescent, inflammatory CD11a^{+} macrophages that accumulated in the brainstem and cerebellum. Blocking MAPK activity and senescence programs reduced peripheral inflammation, brain parenchymal infiltration, neuroinflammation, neuronal damage and improved neurological outcome in preclinical LCH-ND. MAPK activation and senescence programs in circulating myeloid cells represent targetable mechanisms of LCH-ND.

Graphical Abstract
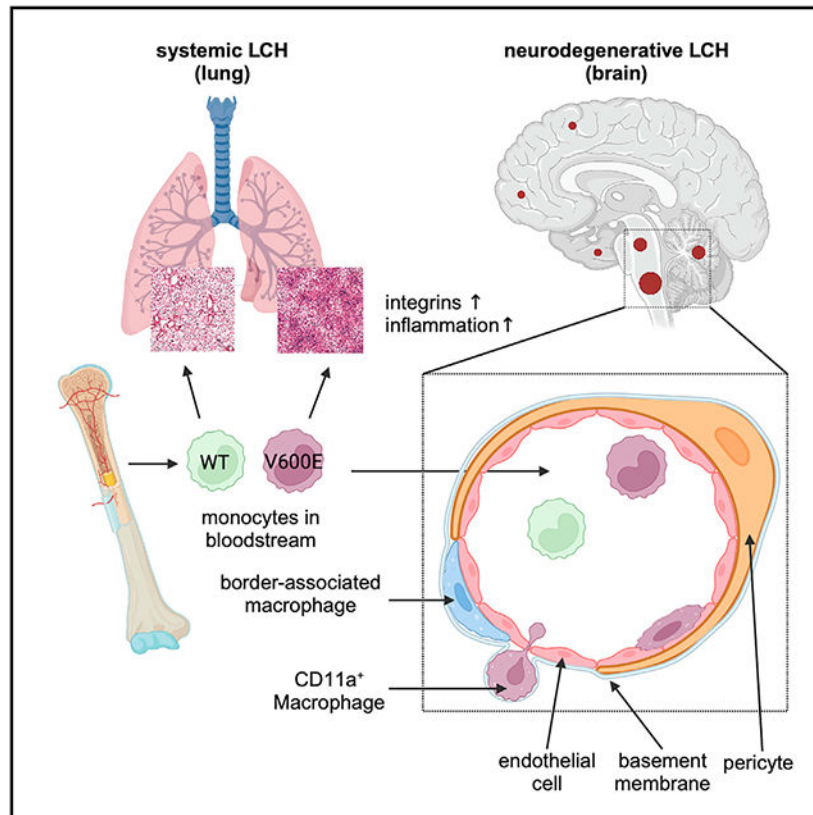
In brief

Patients with Langerhans cell histiocytosis can develop incurable neurodegeneration years after initial systemic disease. Wilk et al. found that MAPK activation in circulating myeloid cells drives a senescent and proinflammatory state that contributes to breakdown of the blood-brain barrier and accumulation of mutant macrophages in the brain. Cognitive and motor deficits can be prevented by MAPK and senolytic Bcl-xL-inhibition.

INTRODUCTION

Neurodegenerative diseases (NDs) are characterized by progressive loss of neuronal function. Mechanisms of ND pathogenesis are incompletely understood, hampering the development of effective therapies. In approximately 10% of patients with Langerhans cell histiocytosis (LCH), a progressive, incurable neuroinflammatory condition LCH-associated neurodegeneration (LCH-ND) arises.[1,2] LCH is an inflammatory neoplastic disorder caused by hematopoietic progenitors expressing mitogen-activated protein kinase (MAPK)-activating mutations that differentiate into senescent mononuclear phagocytes (MNPs) that drive lesion formation.[3,4] LCH therefore represents an informative disease model to investigate mechanisms by which hematopoietic myeloid cells can induce neuroinflammation and neurodegeneration.

LCH-ND is a devastating complication of LCH patients that can arise years after the initial systemic disease is cured. Clinically, LCH-ND is characterized by progressive inflammatory

lesions in the cerebellum, basal ganglia, and brainstem with associated progressive neurologic clinical findings including ataxia, dysarthria and dysmetria.[5] LCH-ND was initially considered a paraneoplastic or autoimmune condition, due to the lack of CD207^{+} cells typically observed in systemic LCH lesions and the presence of T cell infiltrates in the rare cases of reported biopsies.[6,7] Optimal strategies for surveillance and treatment of LCH are poor, and the etiology of LCH-ND remains uncertain. Historically, therapeutic approaches for LCH-ND included observation, immune suppression, and chemotherapy.[1,8,9]

We have previously demonstrated that multisystem LCH is caused by MAPK activating mutations (most commonly *BRAF*V600E) that occur in early hematopoietic progenitors.[10,11] We validated *BRAF*V600E as a driver mutation that recapitulated the LCH phenotype, when expression was enforced in myeloid progenitors.[10] We further demonstrated that the *BRAF*V600E mutation induces an oncogene-driven senescence program in early hematopoietic precursors that reduces their proliferation potential. In these cells, survival is supported by expression of anti-apoptotic molecules such as Bcl-xL and senescence-associated secretory proteins (SASP) that skew the differentiation of *BRAF*V600E[+] hematopoietic progenitors into senescent MNPs that seed peripheral tissues.[3] Senescent MNP that accumulate in tissues drive the formation of inflammatory and granulomatous LCH lesions, leading to tissue damage. Notably, therapies that block SASP and disinhibit resistance to cell death decrease disease burden and prolong survival in mouse models.[3]

The relationship between systemic LCH and LCH-ND is not well defined. There are associations between the risk of developing LCH-ND and disseminated LCH, progressive or relapsed systemic disease, *BRAF*V600E mutation, and lesions in the skull base, the pituitary, and brain parenchyma.[5] Importantly, we recently identified circulating *BRAF*V600E[+] peripheral blood mononuclear cells (PBMC) in the blood of patients with LCH-ND, even in the absence of active systemic lesions. We also detected *BRAF*V600E^{+} myeloid cells in brain biopsies of patients with LCH-ND[3,12] and demonstrated that, similar to peripheral LCH cells, pathogenic MNPs that accumulate in the brain of human LCH-ND exhibit features of senescence.[3] Based on these observations and the clinical patterns of LCH-ND, we hypothesized that LCH-ND arises from hematopoietic precursors that are clonal with peripheral LCH lesions and that senescence programs in infiltrating myeloid cells may also contribute to brain injury in patients with LCH-ND.

Taking advantage of the LCH model of persistent MAPK activation in hematopoietic cells, we sought to define mechanisms by which MAPK activation in MNP could drive neuroinflammation and neurodegeneration. Resident and recruited MNP populations in the central nervous system (CNS) are increasingly recognized to play central roles in a wide range of neurodegenerative conditions[13] by orchestrating immune cell activation. This study highlights a mechanism for monocyte-derived CD11a^{+} macrophages to induce CNS neurodegenerative diseases in histiocytic disorders that can be prevented with MAPK inhibition and senolytic therapy.

RESULTS

Genetic fate-mapping reveals that circulating *BRAF*V600E⁺ myeloid cells accumulate in the brains of mice with LCH-like disease

To study the potential cellular determinants of LCH-ND, we designed transgenic mice that express *BRAF*V600E, the most common somatic mutation in LCH, at different stages of hematopoietic differentiation, recapitulating key features of LCH.[3,10] Specifically, we found that multi-system LCH developed in mice, in which we enforced the *BRAF*V600E mutation under the promoter of the *Scl* gene that is expressed in long-term and short-term hematopoietic stem cells (HSC) in the bone marrow (BM) and showed that *BRAF*V600E⁺ MNPs were the main drivers of tissue injury in the periphery.[3]

To explore whether LCH-ND was also driven by circulating *BRAF*V600E⁺ cells, we used the above model of LCH in which a conditional *BRAF*V600E mutation was enforced under the promoter of the *Scl* gene (Figure 1A). As previously described, we genetically engineered somatic mosaicism for a *BRAF*V600E allele linked to a yellow fluorescent protein (YFP) in HSC using tamoxifen (Tam)-inducible targeting in *Scl*ᶜʳᵉᴱᴿᵀ mice, which we named *BRAF*V600E^Scl, and used *BRAF* wild-type (*BRAF*WT^Scl) as control littermates. Thus, YFP-expressing cells carried the *BRAF*V600E mutation in *BRAF*V600E^Scl mice, whereas YFP-expressing cells in *BRAF*WT^Scl animals did not carry the mutation but underwent Rosa26-locus-driven Cre recombination. Not only did we detect YFP-reporter-tagged, *BRAF*V600E-mutated cells in systemic LCH lesions, we also detected these mutated cells in the brains of *BRAF*V600E^Scl animals beginning around week 8 after tamoxifen-induced cre-recombination and increasing over time (Figures 1B and S1A). We further characterized these cells as CD11a⁺ macrophages, a monocyte-derived population recently described in the CNS vasculature as having the potential to infiltrate brain parenchyma.[14] The population of CD11a⁺ macrophages was the main brain-infiltrating myeloid cell population expressing the *BRAF*V600E mutation in the brains of *BRAF*V600E^Scl mice. This CD11a⁺ macrophage population was enriched up to 50-fold compared to control animals. *BRAF*V600E⁺ cells were notably not detected in either microglia or CD206⁺ border-associated macrophages (BAMs) (Figure 1B). The population of CD206⁺ BAMs comprises parenchymal perivascular macrophages, pial meningeal macrophages, dural macrophages embedded in the falx, and choroid plexus macrophages. The percentage of YFP-tagged cells in the brains of mice correlated with the percentage of reporter-tagged cells in the peripheral blood and was significantly higher in *BRAF*V600E^Scl animals compared to *BRAF*WT^Sc animals (Figure 1C).

To confirm that the *BRAF*V600E⁺ macrophages that accumulated in the brain of *BRAF*V600E^Scl animals arose from circulating precursors and not locally, we developed another model of MAPK activating mutations expressed exclusively in BM HSC by enforcing *BRAF*V600E mutation under the *Map17* gene promoter known to be expressed in long-term bone marrow HSC, which we refer to as *BRAF*V600E^Map17 mice (Figure 1A).[15] Similar to the *BRAF*V600E^Scl model, *BRAF*V600E^Map17 mice developed systemic LCH lesions (Figures S1B and S1C), again emphasizing that multisystem LCH is a myeloid inflammatory neoplasm driven by MAPK-activating mutation expressed in early

HSC.[4] Similar to *BRAF*V600E^{Scl} mice, we detected a large population of *BRAF*V600E$^+$ CD11a$^+$ macrophages in the brain parenchyma of *BRAF*V600E^{Map17} mice between week 12 and 16 after tamoxifen-induced Cre recombination (Figures S1D and S1E), suggesting that circulating *BRAF*V600E$^+$ myeloid cells indeed give rise to *BRAF*V600E$^+$ CD11a$^+$ macrophages.

To further ensure that *BRAF*V600E$^+$ CD11a$^+$ macrophages that accumulated in the brain of these mice derived from circulating mutated cells and did not arise locally, we generated BM chimeric animals (CD45.2 *BRAF*V600E^{Scl}:CD45.1 wild type) in which BM cells isolated from *BRAF*V600E^{Scl} or lineage tracing control mice (*BRAF*WT^{Scl}) were injected into CD45.1$^+$ congenic host mice (Figure 1D). In order to prevent damage to the blood-brain barrier (BBB) induced by pre-transplant conditioning that could artifactually promote translocation of circulating cells into the brain parenchyma, host mice were irradiated with a lead head-shield, as previously described.[16] We found that similar to transgenic mice, chimeric mice also developed systemic LCH lesions (Figures S1F and S1G) as well as brain lesions with accumulation of *BRAF*V600E CD11a$^+$ macrophages (Figures 1E and S1H-S1L). Low numbers of Ly-6Chi monocytes and neutrophils were detected as well (Figures S1I and S1J). Further, *BRAF*V600E^{Scl} mice showed higher numbers of T cells in the brain (Figure S1K). CD11a$^+$ macrophages originated from the donor BM (CD45.2$^+$) and expressed high levels of the cell type-defining integrin alpha L (CD11a) but lacked the expression of markers of CD206$^+$ BAMs (e.g., CD169, LYVE-1, CD206) and showed modest induction of tissue resident microglia markers (e.g., P2RY12) (Figure 1F), confirming that these cells do not present cues of local resident origin. Spatial patterns showed pronounced accumulation of mutated cells in the cerebellum (Figure S1L). Of note, chimeric mice transplanted with BM from *BRAF*WT^{Scl} and *BRAF*V600E^{Scl} donor mice did not differ in terms of donor chimerism (Figure S1M).

We next sought to determine whether CD11a$^+$ macrophages remained restricted to the vasculature or had the potential to invade the brain parenchyma. We intravenously injected *BRAF*V600E^{Scl} mice with an anti-CD45 antibody conjugated to a fluorescent dye to tag intravascular cells prior to brain isolation and analysis (Figure 1G). Nearly 50% of brain-associated CD11a$^+$ macrophages were unstained, suggesting that a substantial fraction of the CD11a$^+$ macrophages while derived from the blood circulation had extravasated into the brain parenchyma of *BRAF*V600E^{Scl} mice (Figure 1H).

LCH mice with brain-infiltrating *BRAF*V600E-mutated cells share phenotypic and transcriptional characteristics with human LCH-ND

In humans, imaging studies and clinical features typically localize LCH lesions and CNS injury to the brainstem (pons, medulla oblongata) and cerebellum as well as to areas with limited BBB (pituitary, vermis, choroid plexus).[5] We recently reported enrichment of *BRAF*V600E$^+$ cells in brainstem and cerebellum with minimal infiltration in the temporal and frontal lobes of a whole brain autopsy from a young man who died from progressive LCH-ND[17] (Figures 2A, 2B, S3A, and S3B). The pattern of neurodegeneration in human LCH-ND matched the main sites of parenchymal infiltration in the *BRAF*V600E^{Scl} chimera. We validated this finding with immunohistochemistry (IHC) and immunolabeling-

enabled three-dimensional imaging of solvent-cleared organs (iDISCO+) and observed an accumulation of *BRAF*V600E-mutated cells primarily in the cerebellum (Figures 2C, 2D, and S1L; Table S2) and also in other parts of the brain including the hippocampus, the choroid plexus (Figures 2C-2D and S2A), and the meninges (Figure S2B). By comparison, the brain infiltration pattern in our *BRAF*V600E[Scl] chimera was diffuse with a lack of granulomatous lesions (Figure 2E, right). By comparison, reporter-tagged cells were virtually absent in brain tissue from the control chimera (Figure 2E, left, and S2A-S2C).

To further establish the pathogenic role of BM-derived *BRAF*V600E^{+} CD11a^{+} macrophages, we obtained and profiled purified CD11a^{+} macrophages, peripheral blood monocytes, and microglia from symptomatic *BRAF*V600E[Scl] and respective *BRAF*WT[Scl] control mice 10–12 weeks after tamoxifen induction. Using bulk RNA sequencing (bulk RNA-seq) from one run of pooled mouse brains, we compared the mRNA transcriptome profiles of each myeloid cell subset from *BRAF*WT[Scl] and *BRAF*V600E[Scl] mice (Figures 2F-2H; Table S1) and generated a deviance score to represent the divergence of gene expression driven by the *BRAF*V600E mutation, wherein a score of 0 would indicate complete concordance between genotypes (Figure 2I). We found that the transcriptomic differences observed in mutant versus wild-type CD11a^{+} macrophages were the most pronounced compared to that computed for *BRAF*V600E^{+} and wild-type monocytes and microglia (Figure 2I), suggesting that the induction of the MAPK pathway activation by *BRAF*V600E substantially impacts the molecular phenotype of the CD11a^{+} macrophages, in line with the anticipated effect of Cre recombination in *BRAF*V600E[Scl] mice. Of note, while monocytes from *BRAF*V600E[Scl] mice harbored the *BRAF*V600E mutation, microglia from *BRAF*V600E[Scl] mice id not.

We had previously shown that an oncogene-induced senescence program is the driver of inflammation in CD207^{+} cells that infiltrate systemic LCH lesions.[3] Thus, we measured the expression of canonical senescence genes in wild-type and *BRAF*V600E CD11a^{+} macrophages and confirmed upregulation of senescence-related genes in *BRAF*V600E[Scl] CD11a^{+} macrophages compared to wild-type cells. Among these upregulated genes, we identified cell cycle control genes encoding the anti-apoptotic Bcl-2 family member Bcl-xL (*Bcl2l1*), uPAR (*Plaur*), and matrix metalloproteinases, which are all classically upregulated during oncogene-induced senescence (Figure 2J). In addition, *BRAF*V600E^{+} CD11a^{+} macrophages overexpressed several integrin sub-units in addition to αL (CD11a, *Itgal*) including subunits α4 (*Itga4*), α5 (*Itga5*), α6 (*Itga6*), and β1 (*Itgb1*), suggesting a potential role for this integrin program in mediating infiltration of brain tissue by *BRAF*V600E^{+} CD11a^{+} macrophages (Figure 2K). CXCR4 was expressed on CD11a^{+} macrophages, in line with our observation that these are BM-derived cells (Figure 2K). We also compared this transcriptional dataset to a case of LCH-ND, for which an RNA-seq dataset is publicly available.[18] Consistent with our observations in mice, we found that mRNA expression of the lineage genes depicted in Figure 2K was more enriched in human LCH-ND, than in bulk profiling of healthy human brain myeloid cells (Figure 2L). In a more comprehensive analysis, we generated a shared mRNA library between our murine bulk RNA-seq dataset from CD11a^{+} macrophages from *BRAF*V600E[Scl] mice with the published dataset of healthy and LCH-ND brain tissue—akin to published strategies applied for single-cell transcriptomic datasets.[19,20] We compared the expression patterns of genes that are enriched

in murine $BRAF$V600E$^+$ CD11a$^+$ macrophages to their wild-type counterparts, with those differentially expressed between human LCH-ND and healthy human brain tissue. From this homology analysis, we found that nearly 60% of genes enriched in $BRAF$V600E$^+$ CD11a$^+$ macrophages are also more highly expressed in human LCH-ND, indicating significant concordance between the transcriptional activity between human LCH-ND and brain infiltration by CD11a$^+$ macrophages in our mouse model (Figure 2M), supporting the likely contribution of the gene program of CD11a$^+$ macrophages in human LCH-ND, analogous to its role in our murine model of LCH-ND.

$BRAF$V600E^{Scl} chimera have a compromised BBB and exhibit behavioral and neurologic abnormalities

Systemic inflammation has been shown to alter the BBB and promote the extravasation of circulating myeloid cells into the brain.[13] Because senescence and systemic inflammation are hallmark features of LCH, we sought to examine whether BBB is altered in mice with multisystem LCH. Consistent with patterns of systemic inflammation in LCH, we found elevated pro-inflammatory cytokines in the brains of $BRAF$V600E^{Scl} chimera as compared to their wild-type counterparts (Figures 3A and 3B). We next compared the fold-change increase from wild-type-baseline of these cytokines between brain and blood and found that matrix metalloproteinase 3 (MMP3) and MMP8 as well as osteopontin were more enriched in the brain than in the serum, while CCL-2, tumor necrosis factor α (TNF-α), and interleukin 1β (IL-1β) were both increased in serum and the brain (Figure 3C). To measure if systemic inflammation was associated with increased BBB leakage in our model, we intravenously injected LCH animals with the albumin-bound Evans Blue dye and measured its extravasation into the brain parenchyma. We found significantly increased dissemination of Evans Blue throughout the brains of LCH mice compared to that of control animals, indicative of an altered BBB that enabled the translocation of small molecules (Figures 3D and 3E). To directly measure an active translocation of blood-derived cytokines, we intravenously injected $BRAF$V600E^{Scl} and $BRAF$WT^{Scl} control animals with a biotinylated version of the inflammatory cytokine IL-1β in $BRAF$V600E^{Scl} mice and $BRAF$WT^{Scl} control animals. We used an avidin-bound fluorescent dye to measure the accumulation of translocated IL-1β in the brain parenchyma of injected mice. Importantly, we found a significant increase of extravasated IL-1β in the brain of LCH mice compared to control mice establishing the increased permeability of the BBB in LCH mice (Figures 3F-3H).

To further investigate the breakdown of BBB in LCH mice, we measured the pericyte coverage of blood vessels in the brains of $BRAF$V600E^{Scl} and $BRAF$WT^{Scl} chimera as a surrogate of BBB integrity (Figure 3I). Accordingly, we documented significantly reduced pericyte coverage of the BBB of $BRAF$V600E^{Scl} chimera relative to $BRAF$WT^{Scl} chimera, indicating a breakdown of the BBB that likely facilitated the extravasation of inflammatory cytokines such as IL-1β and the migration of BM-derived $BRAF$V600E-mutated cells into the brain parenchyma (Figures 3J and S3C).

To assess the pathogenic consequence of the BBB breakdown and increased extravasation of inflammatory cytokines and myeloid cells in the brain parenchyma of LCH mice, we measured the behavioral and neurological phenotypes of $BRAF$V600E^{Scl} chimera using a

range of behavioral tests (Figure 3K). We evaluated murine behavior in an Open Field Assay and found that *BRAF*V600E^{Scl} chimera performed worse compared to control chimera in most relevant parameters such as increase in resting time (Figure 3L), decreased total distance traveled (Figure 3M), and reduced time in center and a lower median velocity (Figures 3N-3P). Using a rotarod assay, we found that *BRAF*V600E^{Scl} chimera have reduced grip strength and a shorter latency to fall compared to wild-type mice (Figures 3Q and 3R), suggesting profound motor deficits in LCH mice. Because CD11a$^+$ macrophages mostly accumulated in the cerebellum, we further focused on motor function assays. Using a footprint assay, we observed a significantly shortened hindlimb and forelimb stride length (Figures 3S and 3T) and a trend toward a broader hind- and forelimb base (Figures 3U and 3V). Sporadic cases of unilateral paralysis were also observed (Figure 3W). Using multiplex immunohistochemistry staining, we also measured Purkinje cell density and found a significant loss of Purkinje cells in *BRAF*V600E^{Scl} chimera (Figure 3X). We further observed a significant increase in GFAP$^+$ areas in the brains of *BRAF*V600E^{Scl} chimera (Figure 3Y) as well as astrocyte activation in close proximity to *BRAF*V600E-mutated cells in the brain of *BRAF*V600E^{Scl} chimera (Figure 3Z). We also detected signs of myelin breakdown in the cerebellum of *BRAF*V600E^{Scl} chimera (Figure S3D) in line with the behavioral and neurological phenotypes observed in these mice.

Accumulation of circulating *BRAF*V600E$^+$ cells is a driver of LCH-like disease, and combined senolytic/MAPK inhibitor therapy alleviates the disease burden

Bcl-xL is highly expressed in systemic LCH lesions, and we have previously shown that treatment of *BRAF*V600E^{Scl} mice with the senolytic Bcl-xL inhibitor navitoclax can deplete LCH cells.[3,11] We previously established a synergistic effect of adding the Bcl-xL inhibitor navitoclax to the MEK inhibitor trametinib (Figures S3E and S3F). We found that while trametinib led to a clinical improvement of mice with a normalization of spleen and liver weight, the treatment did not impact the number of YFP-tagged *BRAF*V600E-mutated cells in organs. In contrast, the Bcl-xL inhibitor navitoclax led to a reduction in YFP$^+$-cell burden but did not consistently exert a relevant effect on organ weights and sizes. Combination treatment, however, alleviated both organ weights and mutated cell burden (Figures S3G and S3I). We therefore tested the ability of MAPK pathway inhibition (trametinib [T], MEK inhibitor) and senolytic therapy (navitoclax [N], Bcl-xL inhibitor) to prevent the accumulation of mutant CD11a$^+$ macrophages in the brain and the associated neuroinflammation (Figures 4A and 4D). MAPK pathway inhibition monotherapy has become a mainstay in relapsed and refractory LCH, but fails to eradicate the LCH clone in mice and humans; it is also less effective in LCH-ND compared to systemic LCH.[21,22] In this study, combining MEK inhibition (T) and Bcl-xL inhibition (N) led to a normalization of the body weight of mice (Figure S3G), spleen size (Figures S3F and S3I), and a substantial reduction of LCH cells in the lungs of mice (Figures 4B and S3I). Importantly, we also found that MEK inhibition and Bcl-xL inhibition (NT) led to a substantial reduction of CD11a$^+$ macrophages in the brain parenchyma mice of transgenic *BRAF*V600E^{Scl} mice (Figure 4C). We confirmed a beneficial effect of the NT combination therapy in *BRAF*V600E^{Scl} chimera with a significant reduction of pathologically increased liver and spleen weight, which become infiltrated with mutant cells in disseminated LCH (Figures 4D-4F). Treatment with the NT combination also prevented the behavioral impairment

observed in LCH mice with an improved performance in across parameters of the Open Field Assay (Figures 4G-4K, top and middle rows). This observation correlates with a trend toward an improved pericyte coverage (Figure S3H) and also with a reduced accumulation of mutant cells in the brains of these mice (Figure 4K, bottom row).

DISCUSSION

LCH-ND is a devastating condition that arises in >10% of patients following the development of systemic LCH. In the most severe cases, patients develop progressive dysarthria, dysmetria, and ataxia that causes significant morbidity and can lead to death.[5] The etiology of LCH-ND has been historically poorly defined. In the past decades, the few brain biopsies studied showed inflammatory cells but lacked CD207^{+} cells characteristic of systemic LCH lesions and granulomatous brain lesions.[6,7] LCH-ND was therefore considered a paraneoplastic or autoimmune phenomenon and typically treated with immunomodulatory therapies (e.g., intravenous immune globulin [IVIG]). Importantly, we identified *BRAF*V600E^{+} cells in the brain biopsies of LCH-ND.[17] In fact, in a brain autopsy from a young patient with fatal LCH-ND, we found that >10% of cells in brainstem and cerebellum were *BRAF*V600E[+], and anatomic concentration of *BRAF*V600E^{+} cells mirrored distribution of disease identified by T2 hyperintensity on MRI. Further, histology of LCH-ND biopsy and autopsy specimens characterized the perivascular concentration of *BRAF*V600E^{+} cells. We also identified *BRAF*V600E^{+} cells in peripheral blood of patients with LCH-ND (without systemic lesions) but did not identify persistent *BRAF*V600E^{+} cells in peripheral blood of patients cured of systemic LCH and without LCH-ND.[17] Similarly, Mass et al. reported the presence of *BRAF*V600E^{+} cells in brain biopsies from patients with LCH and related disorder Erdheim-Chester Disease (ECD).[23] These findings strongly support a clonal relationship between LCH-ND and systemic LCH. Based on our observations of the presence of circulating *BRAF*V600E^{+} cells in patients with LCH-ND and perivascular distribution of *BRAF*V600E[+] in LCH-ND biopsies, we hypothesized that LCH-ND is caused by circulating, BM-derived myeloid cells clonal with systemic LCH lesion MNPs.[17]

To define the mechanisms of LCH-ND, we evaluated three different mouse models for LCH (*BRAF*V600E[Scl], *BRAF*V600E[Map17], *BRAF*V600E[Scl] chimera) in which *BRAF*V600E is post-natally enforced in HSCs. Of note, when we expressed *BRAF*V600E under the CD207 (Langerin) promotor that is transcribed in Langerhans cells of the skin, no circulating mutated cells and no LCH-ND-like phenotype were observed.[24] All of the above-mentioned mice developed aggressive systemic LCH-like disease with risk-organ involvement. We found that circulating *BRAF*V600E^{+} cells infiltrated the brain parenchyma in late-stage disease in all three models, similar to the paradigm in human disease. LCH-ND is typically a late complication of multi-system LCH and typically develops years to decades after the systemic disease has been treated. Recapitulating this sequential pattern and long latency in mouse models is difficult. The advantage and likewise drawback, however, of transgenic mouse models is that the disease burden reflected by the number of circulating mutated cells is higher. In our *BRAF*V600E[Scl] chimera, roughly 10%–20% of all peripheral blood cells expresses the *BRAF*V600E mutation, whereas the burden of circulating cells in human disease varies but is usually in the range below single-digit percentage, mostly

<0.5%.[17] The higher number of circulating *BRAF*V600E$^+$ cells in *BRAF*V600E^{Scl} mice and *BRAF*V600E^{Scl} chimera then allows a more rapid onset of CNS disease that can be studied before the animals succumb to systemic LCH.

We found that human and murine brain manifestations in LCH share similar characteristics, which include (1) a similar distribution pattern of inflammatory cells in the brain parenchyma, (2) the presence of circulating *BRAF*V600E$^+$ myeloid cells expressing a senescence transcriptional program, (3) the presence of inflammatory mediators in the brain parenchyma, and (4) neurological impairment that affects the cerebellum as well as the brain stem. This leads to motor symptoms such as dysdiadochokinesis, ataxia, and dysarthria and a reduction of Purkinje cells as reflected by the behavioral assays performed particularly the footprint assay and is in line with clinical observations in human LCH-ND cases.

Importantly, we found that the accumulation of circulating *BRAF*V600E$^+$ cells was associated with a breakdown of the BBB with increased translocation of inflammatory cytokines and infiltration of circulating senescent *BRAF*V600E$^+$ myeloid cells into the brain parenchyma. We also show that circulating *BRAF*V600E$^+$ myeloid cells differentiated into senescent CD11a$^+$ macrophages within the brain parenchyma. It is likely that cellular senescence of circulating *BRAF*V600E$^+$ myeloid cells and brain-infiltrating *BRAF*V600E$^+$ macrophages contribute to disease progression due to apoptosis resistance and production of senescent associated secretory proteins (SASP) which include inflammatory cytokines such as IL-1, IL-6, and MMPs. Inflammation has long been known to disrupt the BBB and contribute to the pathogenesis of ND.[25,26] MMPs in particular have been shown to be secreted by immune cells leading to a degradation of the basement membrane and subsequent disruption of the BBB.[27] Inflammatory cytokines have also been shown to facilitate the migration of myeloid cells into the brain.[28] While it is difficult to disentangle systemic versus local inflammation as a facilitator of brain infiltration, we found that some inflammatory cytokines (MMPs and osteopontin) are enriched in the brain while others (IL-1β, TNF-α, and CCL-2) are elevated in the blood and in the brain. Notably, osteopontin was the only consistently elevated CSF cytokine in LCH patients with CNS disease compared with patients with other inflammatory and degenerative brain conditions.[17] Importantly, these inflammatory cytokines overlap with classical SASP, and pre-clinical data from LCH mouse models demonstrate that senolytic therapy (e.g., navitoclax), along with MAPK inhibition, may prevent the persistence and differentiation of senescent myeloid cells and subsequent, pathologic neuroinflammation in LCH-ND.

A recent study reported that enforced expression of *BRAF*V600E in erythromyeloid progenitors in mouse embryos leads to progressive neurodegeneration in a mouse model without systemic LCH-like disease and also identified *BRAF*V600E$^+$ cells with a microglia-like phenotype in brain biopsies of patients with neurodegeneration associated with histiocytic disorders.[23] A debate has subsequently developed regarding mechanisms of LCH-ND (and ND associated with related histiocytoses such as ECD) and whether the pathogenic cells invading the brain originate from circulating *BRAF*V600E$^+$ MNP that derived from *BRAF*V600E$^+$ hematopoietic precursors in the BM or from *BRAF*V600E$^+$ microglia that seed the brain during embryonic development. In the typical clinical pattern of LCH-ND, patients first develop systemic LCH, then develop abnormal imaging (T2

hyperintensity on MRI), then some go on to develop clinical features of progressive neurodegeneration.[5] If LCH-ND were microglial in origin, it would be difficult to explain the relationship of LCH-ND with systemic LCH.

Differentiating microglial versus hematopoietic origins of LCH-ND has significant clinical implications on surveillance and therapeutic strategies to prevent and treat LCH-ND. For example, if LCH-ND were microglial in origin, people would be born with intrinsic and unavoidable disease. Treatment would be directed at removing and replacing the mutated tissue resident microglia. By contrast, if LCH-ND arose from hematopoietic cells, surveillance and therapy would aim to identify patients with systemic LCH who are at risk, then prevent accumulation of migrating cells from periphery. A BM-derived pathogenesis paradigm requires a treatment goal of molecular negativity in measurable residual disease (MRD), as is typical for malignant hematologic diseases. The ability of post-natal $BRAF$V600E$^+$ myeloid precursors to recapitulate cellular and clinical features of LCH-ND—and the identification of $BRAF$V600E$^+$ PBMC and the perivascular localization of $BRAF$V600E$^+$ CXCR4$^+$ myeloid cells in the brain of human LCH-ND—strongly support a hematopoietic origin of cellular drivers of LCH-ND. We previously reported that the extent of disease in LCH is determined by the differentiation state of the myeloid precursors in which the $BRAF$V600E mutation (or alternative activating MAPK pathway mutations) arise.[10] The patterns of disease associated with LCH-ND (e.g., disseminated LCH, lesions in skull base and facial bones, and pituitary involvement[5]) may represent $BRAF$V600E in myeloid precursors with potential to develop into both CD207$^+$ DC-like cells (systemic lesions) and monocyte-derived CD11a$^+$ macrophages (LCH-ND). Currently, "cure" with MRD negativity is sometimes achieved by chemotherapy but rarely achieved by MAPK inhibitor treatment alone, even in cases with positive clinical responses.[22,29] Patients with resolution of systemic lesions but persistent $BRAF$V600E$^+$ peripheral blood clone could remain at risk for the development of LCH-ND. Therefore, CD11a$^+$ macrophage represents a Trojan horse and a potential therapeutic target, responsible for trafficking LCH disease to the CNS.

The mouse models and treatment approaches developed in this study not only transform our understanding of LCH-ND pathophysiology, but also pave the way for future preventive and therapeutic treatment trajectories for LCH-ND. Beyond LCH, MAPK activation in monocyte precursors could be more broadly relevant in driving neuroinflammation in conditions such as infections or age-associated clonal hematopoiesis, where MAPK activation in monocytes from a variety of stimuli may prompt differentiation into senescent CD11a$^+$ macrophages, invasion of the BBB, and neuroinflammation.

Limitations of the study

Primary patient material from patients with LCH-ND is rare. Therefore, the human IHC shown in this work stems from one patient. Likewise, the human bulk RNA-seq dataset used in this study is obtained from one patient with LCH-ND. While the clinical phenotype as well as the histological and transcriptional patterns between the human samples and the mouse model are similar, future studies are needed for additional comparison between human LCH-ND and the mouse models described in this work.

STAR★METHODS

RESOURCE AVAILIBILITY

Lead contact—Further information and requests for resources and reagents should be directed to and will be fulfilled by the lead contact, Miriam Merad (miriam.merad@mssm.edu).

Materials availability—The study did not generate new unique reagents.

Data and code availability

1. Datasets supporting the findings presented in this study will be provided by the Lead contact upon request. Any data will be released via a material transfer agreement. Bulk RNA-seq data obtained from mouse brain macrophages have been deposited in GEO and are publicly available from the date of publication. Accession numbers are listed in the Key Resources Table.

2. This paper does not report original code.

3. Any additional information required to reanalyze the data reported in this paper is available from the lead contact upon request.

EXPERIMENTAL MODEL AND STUDY PARTICIPANT DETAILS

Mice—*BRAF*V600E$^{HSC–Scl-CreERT}$xR26$^{YFP/−}$ mice (*BRAF*V600E^{Scl} mice) and *BRAF*WT$^{HSC–Scl-CreERT}$xR26$^{YFP/−}$ mice (*BRAF*WT^{Scl} control mice) were generated as described previously.[3] *BRAF*V600E$^{ca/ca}$ mice were bred with R26$^{YFP/YFP}$ mice and offspring mice were bred to homozygosity for YFP and heterozygosity for *BRAF*V600E. The resulting mice were bred with HSC-Scl^{CreERT} mice to obtain either *BRAF*V600E^{Scl} mice or *BRAF*WT^{Scl} control mice. Female and male mice were used for all studies unless for chimera, where male donors and male recipients were chosen. All mice were 6–8 weeks of age at the time of experiment start, recipient mice for chimera were 6–8 weeks old at transplantation. To induce recombination in these mice, 5 doses of tamoxifen were given on 5 consecutive days (5mg, 2mg, 2mg, 1mg, 1mg) as previously described.[31] *BRAF*V600E^{Scl} mice and *BRAF*WT^{Scl} control mice were terminally analyzed between week 8 and 12 post tamoxifen induction. *BRAF*V600E$^{Map17–CreERT}$xR26$^{tdTomato/−}$ mice (*BRAF*V600E^{Map17} mice) and *BRAF*WT$^{Map17–CreERT}$xR26$^{tdTomato/−}$ mice (*BRAF*WT^{Map17} control mice) were generated by crossing *Map17*$^{creER/+}$*R26tdTomato*$^{+/+}$ (*Pdzk1ip1-creER R26tdTomato*$^{+/+}$)[15,20] mice to *BRAF*V600E$^{ca/WT}$ mice. To induce recombination in *BRAF*V600E^{Map17} mice and *BRAF*WT^{Map17} control mice, 1 dose of 5mg tamoxifen was given as previously described.[15,20] *BRAF*V600E^{Map17} mice and *BRAF*WT^{Map17} control mice were terminally analyzed between week 12 and 16 post tamoxifen induction. BM chimera were generated by transplanting 5x10^6 total BM cells from *BRAF*V600E^{Scl} mice or *BRAF*WT^{Scl} control mice into congenic CD45.1 WT host mice (*BRAF*V600E^{Scl} chimera and *BRAF*WT^{Scl} control chimera). Host mice were irradiated with twice 5.5Gy 6 h apart with a lead shield protecting the head of the host mice in analogy to a previous report.[16] To induce recombination in *BRAF*V600E^{Scl} chimera and *BRAF*WT^{Scl} control chimera, 2 doses of tamoxifen 2mg were given 1 week apart not earlier than 4 weeks after transplantation. Chimera were terminally

analyzed between week 12 and 20 after tamoxifen induction. Ethical approval for mouse experiments was obtained by the Internal Animal Care and Use Committee (IACUC) at the Mount Sinai Hospital.

Human sample—The human sample used stems from an autopsy specimen of an 11-year old male patient with LCH-ND described in McClain et al.[17] Informed consent was obtained and research conducted per Baylor College of Medicine IRB approved protocol.

METHOD DETAILS

Brain macrophage isolation—Brain macrophages were isolated as described previously.[14] Mice were anesthetized with Ketamine/Xylazine and upon areflexia transcardially perfused with PBS. Brains were extracted, cut into small pieces and digested with Collagenase IV 0.2 mg/mL (Sigma, C5138-1G) and DNAse-1 0.05 mg/mL (Sigma, DN25-1G) in RPMI containing 10% FCS[32] for 30 min at 37°C. Digested brains were passed through a 70-μm cell strainer and incubated with magnetic anti-CD45 microbeads (Miltenyi Biotec, #130-052-301) according to the manufacturer's instructions. CD45$^+$ cells were isolated using two consecutive LS columns (Miltenyi Biotec, #130-042-401) per brain and subjected to downstream analyses.

Intravascular staining for discrimination of vascular vs. parenchymal myeloid cells—Discrimination of intravascular vs. extravascular myeloid cells was performed in symptomatic animals 10–12 weeks post tamoxifen induction in analogy to published protocols.[33,34] Mice were anesthetized with Ketamine/Xylazine and 10μL of an anti-mouse CD45 antibody conjugated to BV510 were injected intravenously in a 100μL PBS. 10 min later, mice were anesthetized and perfused with PBS. Brain macrophages were then extracted as described above and stained with respective antibodies containing an anti-mouse CD45 antibody conjugated to AF700.

Spectral cytometry—Brain macrophage single cell suspensions were stained with a fixable blue dead cell stain kit (Thermo Fisher Scientific, L-23105) in PBS for 15min on ice. After one washing cycle in cytometry buffer (PBS containing 10% BSA and 2mM EDTA), each cell sample was resuspended in 50μL of cytometry buffer containing the respective antibodies and complemented with 5μL of Super Bright Complete Staining Buffer (Thermo Fisher Scientific, SB-4401-75). Samples were acquired on a Cytek Aurora full spectrum cytometer (Configuration: 5 Laser - 16UV-16V-14B-10YG-8R). Autofluorescence detection and extraction was applied during unmixing using Cytek SpectroFlo v2.2.0.3 software (Cytek Biosciences, Fremont, CA, USA). Unmixed.fcs files were then analyzed with FlowJo Version 10 (Becton Dickinson, Franklin Lakes, NJ, USA). Gating strategies are displayed in Figure S4. Conditions for the respective antibodies are listed in the Key Resources Table.

Cell sorting—Brain macrophage single-cell suspension and cell staining was performed as described above. Brain samples were then sorted on a Cytek Aurora CS full spectrum cell sorter (Configuration: 5 Laser - 16UV-16V-14B-10YG-8R) with autofluorescence detection and extraction applied during unmixing (Cytek Biosciences, Fremont, CA, USA). The instrument was set up using a 100μm nozzle at 18.3psi using Single Cell sort mode. Cells

were sorted into RNA lysis buffer in 1.5mL tubes. Sorted brain macrophage populations were then subjected to Ultra-low-input RNA sequencing. Conditions for the respective antibodies are listed in the Key Resources Table.

Ultra-low-input RNA-sequencing—RNA extraction, library preparation, sequencing and analysis were completed at Azenta Life Science (South Plainfield, NJ) as follows.

RNA extraction—Total RNA was extracted using Qiagen RNeasy Plus Mini kit following manufacturer's instructions (Qiagen, Hilden, Germany). Extracted RNA samples were quantified using Qubit 2.0 Fluorometer (Life Technologies, Carlsbad, CA, USA) and RNA integrity was checked using Agilent TapeStation 4200 (Agilent Technologies, Palo Alto, CA, USA).

Library preparation—Ultra-low input RNA sequencing library was prepared by using SMART-Seq HT kit for full-length cDNA synthesis and amplification (Takara Bio, San Jose, CA, USA), and Illumina Nextera XT (Illumina, San Diego, CA, USA) library was used for sequencing library preparation. Briefly, cDNA was fragmented, and adaptor was added using Transposase, followed by limited-cycle PCR to enrich and add index to the cDNA fragments. The sequencing library was validated on the Agilent TapeStation (Agilent Technologies, Palo Alto, CA, USA), and quantified by using Qubit 2.0 Fluorometer (Thermo Fisher Scientific, Waltham, MA, USA) as well as by quantitative PCR (KAPA Biosystems, Wilmington, MA, USA).

Sequencing—The sequencing libraries were multiplexed and clustered onto a flowcell. After clustering, the flowcell was loaded onto the Illumina HiSeq instrument according to manufacturer's instructions. The samples were sequenced using a 2x150bp Paired End (PE) configuration. Image analysis and base calling were conducted by the HiSeq Control Software (HCS). Raw sequence data (.bcl files) generated from Illumina HiSeq was converted into fastq files and de-multiplexed using Illumina bcl2fastq 2.20 software. One mis-match was allowed for index sequence identification. After investigating the quality of the raw data, sequence reads were trimmed to remove possible adapter sequences and nucleotides with poor quality using Trimmomatic v.0.36. The trimmed reads were mapped to the Mus musculus reference genome available on ENSEMBL using the STAR aligner v.2.5.2b. BAM files were generated as a result of this step. Unique gene hit counts were calculated by using feature Counts from the Subread package v.1.5.2. Only unique reads that fell within exon regions were counted. After extraction of gene hit counts, the gene hit counts table was used for downstream differential expression analysis.

Analysis—Gene expression was computed as normalized transcript counts per million for individual samples to control for transcript sequencing variability across runs. To assess gene expression patterns across species, homologous genes between mice and humans were identified in the libraries generated for this study and for prior published work (GSE73721 and GSE74442).[18,30] Respective datasets were then subsetted for these homologous genes across samples to compute log normalized gene expression as an integrated dataset. To assess transcriptomic differences driven by induction of the *BRAF*V600E mutation in hematopoietic cells, a deviance score – defined as the orthogonal distance of individual

genes from the line of equality on a Cartesian plane, representative of concordance in mRNA expression – was generated to compute a quantitative description for transcriptomic remodeling.

Immunohistochemistry and multiplexed immunohistochemical consecutive staining on a single slide—Mice were anesthetized with Ketamine/Xylazine as previously described and upon areflexia transcardially perfused with PBS followed by 4% PFA. Brains were extracted and post-fixed in 4% PFA overnight and embedded in paraffin. Multiplexed immunohistochemical consecutive staining on a single slide (MICSSS) was performed as described previously.[35] Conditions for the respective antibodies are listed in the Key Resources Table.

iDISCO+ staining, imaging, and ClearMap analysis—*BRAF*V600E[Map17] and *BRAF*WT[Map17] mice were perfused and brains were extracted and postfixed with 4% PFA in PBS at 4°C for 18h. Brains were then cleared and stained as described in the iDISCO+ staining protocol available at https://idisco.info. Brains were incubated with the primary anti-DsRed antibody cross-reactive with tdTomato (Rockland, #600-501-379, 1:1,000) followed by the corresponding secondary antibody (donkey anti-rabbit IgG, Alexa Fluor 647, Thermo Fisher Scientific, #A-31573, 1:1,000) for 7 days at 37°C. Imaging was conducted using a LaVision lightsheet microscope with zoom body for sagittal half brain scanning with dynamic focus and a z stack thickness of 4μm. Brain images were processed as previously described using ClearMap.[36] tdTomato$^+$ cells were quantified using the cell detection module optimized and validated based on the intensity and shape parameters of the signal. The autofluorescence channel was aligned to the Allen Institute's Common Coordinate Framework using the Elastix toolbox. Brain areas were collapsed into their parent regions prior to analyses.

Luminex multiplexed protein quantification from mouse brains—Brain tissue of perfused mice was dissociated with Pistil A and B and then lysed in ProcartaPlex Cell Lysis buffer (Thermo Fisher Scientific, EPX-999-000) with Halt Protease Inhibitor Cocktail (Thermo Fisher Scientific, #78430). Samples were spun down at 20,000xg for 10 min. Supernatants were frozen at −80°C until further processing. Samples were run on the FlexMap3D Luminex machine according to the manufacturer's recommendations using the following Millipore panels: MKI2MAG-94K, MMMP1MAG-79K, MHSTCMAG-70KPXBK, MMMP2MAG-79K (Millipore Sigma, Burlington, MA, USA).

Evans blue assay—*BRAF*V600E[Scl] mice and *BRAF*WT[Scl] control mice were intravenously injected with 6 μL/g body weight of Evans Blue 2% in 0.9% saline. 16 h later, animals were anesthetized with Ketamine/Xylazine and transcardially perfused with 25mL of PBS. Brains were then weighed and 400μL of dimethylformamide was added to the 1.5mL tube containing the brain and dissociated. Brains were incubated at 55°C for 48h and vortexed once daily. Samples were then spun down at 21,000g for 30min and supernatant was analyzed on a photometer with an excitation of 620nm and Emission of 680nm with an appropriate control standard curve.

Quantification of vessel pericyte coverage—Brain blood vessel coverage with pericytes was investigated as described previously.[37] Mice were perfused with PBS followed by 4% PFA using a gravity perfusion approach (20cm gradient and 1.2mm tube diameter). Brains were post fixed overnight in 4% PFA and then cut on a vibratome in 60μm thick sections. Free-floating tissue sections were permeabilized overnight in permeabilization buffer (1% BSA, 2% Triton X-100 in PBS) at 4°C. Primary antibodies directed against Collagen IV (Bio-Rad, #2150-1470, 1:300) and Aminopeptidase N/ CD13 (R&D Systems, AF2335,1:100) were incubated for 48 h followed by secondary antibodies (Cy5-conjugated AffiniPure Donkey Anti-Goat IgG #705-175-147 and DyLight488 AffiniPure Donkey Anti-Rabbit IgG #711-485-152, dilution 1:300, Jackson Immuno Research) for 24 h. Tissue sections were mounted using Molecular Probes ProLong Gold Antifade Mountant (Thermo Fisher Scientific, #P36930). Conditions for the respective antibodies are also listed in the Key Resources Table. Images of immune-fluorescently labeled sections were acquired by Zeiss LSM780 confocal laser scanning microscope with a 20X objective (Zeiss, Oberkochen, Germany). Pericyte coverage was calculated using the area measurement tool in Fiji. The area of CD13 and Collagen IV signal was measured on binary images in 6 ROIs, 100×100 μm each, in sagittal brain section. Coverage was calculated as the percentage of CD13 positive area over the Collagen IV positive area. The Collagen IV area was taken arbitrarily as 100% and the CD13 positive area was expressed as a percentage normalized to the Collagen IV area.

Biotinylation—Biotinylation of recombinant IL-1β (R&D Systems, 201-LB-025/CF) was performed using the EZ-Link Sulfo-NHS-Biotin kit according to the manufacturer's instructions (Thermo Fisher Scientific, #A39256). Biotinylated IL-1β was separated from unbound biotin using Pierce C18 Spin Columns, 7K MWCO, (Thermo Fisher Scientific, #89870), which recovers proteins and macromolecules larger than 7kDa. 100μL of biotinylated IL-1β was injected retro-orbitally into anesthetized mice at a concentration of 250 ng/ml. After 2 h of circulation, mice were euthanized and perfused with ice-cold PBS followed by 4% PFA. Brain tissue processing and imaging was performed as described in the Pericyte coverage section. Biotin was visualized using the Oregon Green 488 conjugate of NeutrAvidin biotin-binding protein (Thermo Fisher Scientific, #A6374). Counterstaining was performed using rabbit anti-Collagen IV (1:300, Bio-Rad, #2150-1470). Conditions for the respective antibodies are also listed in the Key Resources Table.

Open Field Assay—*BRAF*V600E^Scl chimera and *BRAF*WT^Scl chimera were studied for abnormal behavior in an Open Field assay. Therefore, movement of mice was tracked in an open field chamber for 60 min during the night cycle after acclimatization to red light for 1 h. Data were analyzed using the proprietary software of the Open Field chambers (Omnitech Electronics, Fusion 5.6).

Grip strength analysis—*BRAF*V600E^Scl chimera and *BRAF*WT^Scl control chimera were tested for grip strength using a grip strength meter (Biosep, Bio-GS3) as suggested by the manufacturer. Mice were trained on the setup before grip strength was assess in 3 consecutive rounds including appropriate breaks between sessions. Mean values of the peak grip force of each mouse were used for statistical analysis.

Rotarod assay—*BRAF*V600E^{Scl} chimera and *BRAF*WT^{Scl} chimera were evaluated for ataxia using an accelerating rotating rod (Rotarod) setup.[38] The animals were placed on the rotating rod an acceleration from 4 to 40rpm was initiated. Latency to fall from the rod was recorded after training runs. In total 3 recorded sessions were analyzed and mean latency to fall plotted.

Footprint analysis—*BRAF*V600E^{Scl} chimera and *BRAF*WT^{Scl} control chimera were investigated for cerebellar ataxia using a footprint assay as previously described.[39] The hind paws of experimental mice were painted with a non-toxic blue color, while the front paws were painted with red color. The mice were then given the opportunity to run along a corridor lined with paper into a darkened box. The gait of the hind and front paws, as well as the stride length, were then measured.

***In vivo* drug treatment**—*BRAF*V600E^{Scl} mice and *BRAF*WT^{Scl} control mice as well as *BRAF*V600E^{Scl} chimera and *BRAF*WT^{Scl} control chimera were treated with navitoclax at a dose of 50 mg/kg daily by oral gavage (ApexBio, #A3007)[3] in combination with trametinib 1 mg/kg daily intraperitoneally (i.p.) (Selleck Chemicals, #S2673)[40] for 8 weeks before terminal analysis.

QUANTIFICATION AND STATISTICAL ANALYSIS

Statistical significance between groups was determined by unpaired Student's *t* test or one-sided ANOVA; data are displayed as means ± s.e.m. Statistical analysis was done with GraphPad Prism v.9.3.

Supplementary Material

Refer to Web version on PubMed Central for supplementary material.

ACKNOWLEDGMENTS

REFERENCES

1. Allen CE, Flores R, Rauch R, Dauser R, Murray JC, Puccetti D, Hsu DA, Sondel P, Hetherington M, Goldman S, and McClain KL (2010). Neurodegenerative central nervous system Langerhans cell histiocytosis and coincident hydrocephalus treated with vincristine/cytosine arabinoside. Pediatr. Blood Cancer 54, 416–423. [PubMed: 19908293]

2. Héritier S, Barkaoui MA, Miron J, Thomas C, Moshous D, Lambilliotte A, Mazingue F, Kebaili K, Jeziorski E, Plat G, et al. (2018). Incidence and risk factors for clinical neurodegenerative Langerhans cell histiocytosis: a longitudinal cohort study. Br. J. Haematol 183, 608–617. [PubMed: 30421536]

3. Bigenwald C, Berichel JL, Wilk CM, Chakraborty R, Chen ST, Tabachnikova A, Mancusi R, Abhyankar H, Casanova-Acebes M, Laface I, et al. (2021). BRAFV600E-induced senescence drives Langerhans cell histiocytosis pathophysiology. Nat Med 27, 851–861. [PubMed: 33958797]

4. Allen CE, Merad M, and McClain KL (2018). Langerhans-Cell Histiocytosis. N. Engl. J. Med 379, 856–868. [PubMed: 30157397]

5. Yeh EA, Greenberg J, Abla O, Longoni G, Diamond E, Hermiston M, Tran B, Rodriguez-Galindo C, Allen CE, and McClain KL; North American Consortium for Histiocytosis (2018). Evaluation and treatment of Langerhans cell histiocytosis patients with central nervous system abnormalities: Current views and new vistas. Pediatr. Blood Cancer 65, e26784.

6. Grois N, Prayer D, Prosch H, and Lassmann H; CNS LCH Co-operative Group (2005). Neuropathology of CNS disease in Langerhans cell histiocytosis. Brain 128, 829–838. [PubMed: 15705614]

7. Grois N, Tsunematsu Y, Barkovich AJ, and Favara BE (1994). Central nervous system disease in Langerhans cell histiocytosis. Br. J. Cancer Suppl 23, S24–S28. [PubMed: 8075002]

8. Idbaih A, Donadieu J, Barthez MA, Geissmann F, Bertrand Y, Hermine O, Brugières L, Genereau T, Thomas C, and Hoang-Xuan K (2004). Retinoic acid therapy in "degenerative-like" neuro-langerhans cell histiocytosis: A prospective pilot study. Pediatr. Blood Cancer 43, 55–58. [PubMed: 15170890]

9. Imashuku S, Fujita N, Shioda Y, Noma H, Seto S, Minato T, Sakashita K, Ito N, Kobayashi R, and Morimoto A; Japan LCH Study Group JLSG (2015). Follow-up of pediatric patients treated by IVIG for Langerhans cell histiocytosis (LCH)-related neurodegenerative CNS disease. Int. J. Hematol 101, 191–197. [PubMed: 25491495]

10. Berres M-L, Lim KPH, Peters T, Price J, Takizawa H, Salmon H, Idoyaga J, Ruzo A, Lupo PJ, Hicks MJ, et al. (2014). BRAF-V600E expression in precursor versus differentiated dendritic cells defines clinically distinct LCH risk groupsLCH: neoplasia arising from myeloid precursors. J. Exp. Med 211, 669–683. [PubMed: 24638167]

11. Hogstad B, Berres M-L, Chakraborty R, Tang J, Bigenwald C, Serasinghe M, Lim KPH, Lin H, Man T-K, Remark R, et al. (2018). RAF/MEK/extracellular signal–related kinase pathway suppresses dendritic cell migration and traps dendritic cells in Langerhans cell histiocytosis lesions. J. Exp. Med 215, 319–336. [PubMed: 29263218]

12. McClain KL, Bigenwald C, Collin M, Haroche J, Marsh RA, Merad M, Picarsic J, Ribeiro KB, and Allen CE (2021). Histiocytic disorders. Nat. Rev. Dis. Primers 7, 73. [PubMed: 34620874]

13. Paolicelli RC, Sierra A, Stevens B, Tremblay M-E, Aguzzi A, Ajami B, Amit I, Audinat E, Bechmann I, Bennett M, et al. (2022). Microglia states and nomenclature: A field at its crossroads. Neuron 110, 3458–3483. [PubMed: 36327895]

14. Silvin A, Uderhardt S, Piot C, Da Mesquita S, Yang K, Geirsdottir L, Mulder K, Eyal D, Liu Z, Bridlance C, et al. (2022). Dual ontogeny of disease-associated microglia and disease inflammatory macrophages in aging and neurodegeneration. Immunity 55, 1448–1465.e6. [PubMed: 35931085]

15. Sawai CM, Babovic S, Upadhaya S, Knapp DJHF, Lavin Y, Lau CM, Goloborodko A, Feng J, Fujisaki J, Ding L, et al. (2016). Hematopoietic Stem Cells Are the Major Source of Multilineage Hematopoiesis in Adult Animals. Immunity 45, 597–609. [PubMed: 27590115]

16. Mildner A, Schmidt H, Nitsche M, Merkler D, Hanisch U-K, Mack M, Heikenwalder M, Brück W, Priller J, and Prinz M (2007). Microglia in the adult brain arise from Ly-6ChiCCR2+ monocytes only under defined host conditions. Nat. Neurosci 10, 1544–1553. [PubMed: 18026096]

17. McClain KL, Picarsic J, Chakraborty R, Zinn D, Lin H, Abhyankar H, Scull B, Shih A, Lim KPH, Eckstein O, et al. (2018). CNS Langerhans cell histiocytosis: Common hematopoietic origin for LCH-associated neurodegeneration and mass lesions: Hematopoietic Origin of LCH-ND. Cancer 124, 2607–2620. [PubMed: 29624648]

18. Diamond EL, Durham BH, Haroche J, Yao Z, Ma J, Parikh SA, Wang Z, Choi J, Kim E, Cohen-Aubart F, et al. (2016). Diverse and Targetable Kinase Alterations Drive Histiocytic Neoplasms. Cancer Discov. 6, 154–165. [PubMed: 26566875]

19. Maier B, Leader AM, Chen ST, Tung N, Chang C, LeBerichel J, Chudnovskiy A, Maskey S, Walker L, Finnigan JP, et al. (2020). A conserved dendritic-cell regulatory program limits antitumour immunity. Nature 580, 257–262. [PubMed: 32269339]

20. Casanova-Acebes M, Dalla E, Leader AM, LeBerichel J, Nikolic J, Morales BM, Brown M, Chang C, Troncoso L, Chen ST, et al. (2021). Tissue-resident macrophages provide a pro-tumorigenic niche to early NSCLC cells. Nature 595, 578–584. [PubMed: 34135508]

21. Cohen Aubart F, Emile J-F, Carrat F, Charlotte F, Benameur N, Donadieu J, Maksud P, Idbaih A, Barete S, Hoang-Xuan K, et al. (2017). Targeted therapies in 54 patients with Erdheim-Chester disease, including follow-up after interruption (the LOVE study). Blood 130, 1377–1380. [PubMed: 28667012]

22. Eckstein OS, Visser J, Rodriguez-Galindo C, and Allen CE; NACHO-LIBRE Study Group (2019). Clinical responses and persistent BRAF V600E+ blood cells in children with LCH treated with MAPK pathway inhibition. Blood 133, 1691–1694. [PubMed: 30718231]

23. Mass E, Jacome-Galarza CE, Blank T, Lazarov T, Durham BH, Ozkaya N, Pastore A, Schwabenland M, Chung YR, Rosenblum MK, et al. (2017). A somatic mutation in erythro-myeloid progenitors causes neurodegenerative disease. Nature 549, 389–393. [PubMed: 28854169]

24. Berres M-L, Lim KPH, Peters T, Price J, Takizawa H, Salmon H, Idoyaga J, Ruzo A, Lupo PJ, Hicks MJ, et al. (2015). BRAF-V600E expression in precursor versus differentiated dendritic cells defines clinically distinct LCH risk groups. J. Exp. Med 212, 281. [PubMed: 25646268]

25. Varatharaj A, and Galea I (2017). The blood-brain barrier in systemic inflammation. Brain Behav. Immun 60, 1–12. [PubMed: 26995317]

26. Takata F, Nakagawa S, Matsumoto J, and Dohgu S (2021). Blood-Brain Barrier Dysfunction Amplifies the Development of Neuroinflammation: Understanding of Cellular Events in Brain Microvascular Endothelial Cells for Prevention and Treatment of BBB Dysfunction. Front. Cell. Neurosci 15, 661838. [PubMed: 34588955]

27. Lakhan SE, Kirchgessner A, Tepper D, and Leonard A (2013). Matrix Metalloproteinases and Blood-Brain Barrier Disruption in Acute Ischemic Stroke. Front. Neurol 4, 32. [PubMed: 23565108]

28. Spath S, Komuczki J, Hermann M, Pelczar P, Mair F, Schreiner B, and Becher B (2017). Dysregulation of the Cytokine GM-CSF Induces Spontaneous Phagocyte Invasion and Immunopathology in the Central Nervous System. Immunity 46, 245–260. [PubMed: 28228281]

29. Donadieu J, Larabi IA, Tardieu M, Visser J, Hutter C, Sieni E, Kabbara N, Barkaoui M, Miron J, Chalard F, et al. (2019). Vemurafenib for Refractory Multisystem Langerhans Cell Histiocytosis in Children: An International Observational Study. J. Clin. Oncol 37, 2857–2865. [PubMed: 31513482]

30. Zhang Y, Sloan SA, Clarke LE, Caneda C, Plaza CA, Blumenthal PD, Vogel H, Steinberg GK, Edwards MSB, Li G, et al. (2016). Purification and Characterization of Progenitor and Mature Human Astrocytes Reveals Transcriptional and Functional Differences with Mouse. Neuron 89, 37–53. [PubMed: 26687838]

31. Göthert JR, Gustin SE, Hall MA, Green AR, Göttgens B, Izon DJ, and Begley CG (2005). In vivo fate-tracing studies using the Scl stem cell enhancer: embryonic hematopoietic stem cells significantly contribute to adult hematopoiesis. Blood 105, 2724–2732. [PubMed: 15598809]

32. Liu Z, Gu Y, Shin A, Zhang S, and Ginhoux F (2020). Analysis of Myeloid Cells in Mouse Tissues with Flow Cytometry. STAR Protoc. 1, 100029. [PubMed: 33111080]

33. Anderson KG, Mayer-Barber K, Sung H, Beura L, James BR, Taylor JJ, Qunaj L, Griffith TS, Vezys V, Barber DL, and Masopust D (2014). Intravascular staining for discrimination of vascular and tissue leukocytes. Nat. Protoc 9, 209–222. [PubMed: 24385150]

34. Hamon P, Loyher P-L, Baudesson de Chanville C, Licata F, Combadière C, and Boissonnas A (2017). CX3CR1-dependent endothelial margination modulates Ly6Chigh monocyte systemic deployment upon inflammation in mice. Blood 129, 1296–1307. [PubMed: 28011675]

35. Remark R, Merghoub T, Grabe N, Litjens G, Damotte D, Wolchok JD, Merad M, and Gnjatic S (2016). In-depth tissue profiling using multiplexed immunohistochemical consecutive staining on single slide. Sci. Immunol 1, aaf6925. [PubMed: 28783673]

36. Renier N, Adams EL, Kirst C, Wu Z, Azevedo R, Kohl J, Autry AE, Kadiri L, Umadevi Venkataraju K, Zhou Y, et al. (2016). Mapping of Brain Activity by Automated Volume Analysis of Immediate Early Genes. Cell 165, 1789–1802. [PubMed: 27238021]

37. Török O, Schreiner B, Schaffenrath J, Tsai H-C, Maheshwari U, Stifter SA, Welsh C, Amorim A, Sridhar S, Utz SG, et al. (2021). Pericytes regulate vascular immune homeostasis in the CNS. Proc National Acad Sci 118, e2016587118.

38. Brooks SP, and Dunnett SB (2009). Tests to assess motor phenotype in mice: a user's guide. Nat. Rev. Neurosci 10, 519–529. [PubMed: 19513088]

39. Sugimoto H, and Kawakami K (2019). Low-cost Protocol of Footprint Analysis and Hanging Box Test for Mice Applied the Chronic Restraint Stress. J. Vis. Exp 10.

40. Sengal A, Velazquez J, Hahne M, Burke TM, Abhyankar H, Reyes R, Olea W, Scull B, Eckstein OS, Bigenwald C, et al. (2021). Overcoming T-cell exhaustion in LCH: PD-1 blockade and targeted MAPK inhibition are synergistic in a mouse model of LCH. Blood 137, 1777–1791. [PubMed: 33075814]

Highlights

- MAPK activation in BM-derived CD11a$^+$ macrophages drives neurodegeneration in LCH mice

- Similar spatial and transcriptional patterns between mouse and human CNS LCH

- LCH mice have a leaky BBB and enhanced CNS inflammation

- Senolytic treatment prevents neurodegenerative phenotype in LCH mice
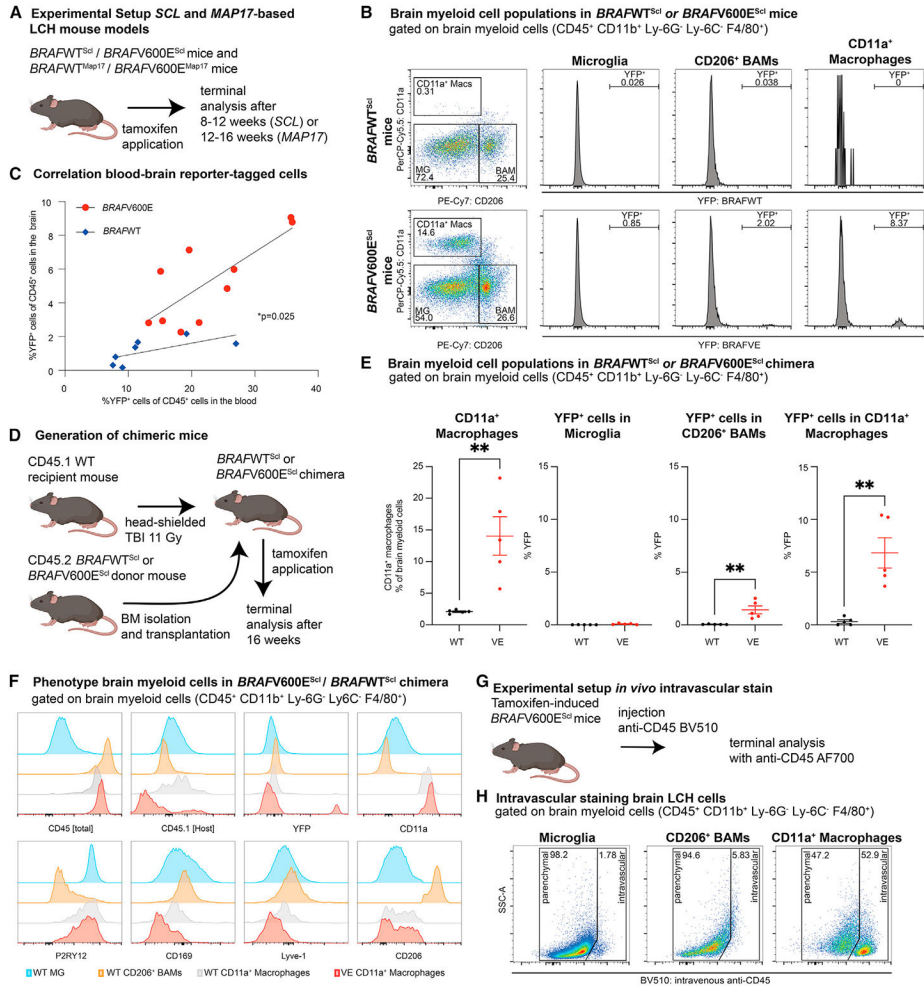
Figure 1. Genetic fate-mapping reveals that circulating *BRAF*V600E+ myeloid cells accumulate in the brains of mice with LCH-like disease

(A) Experimental setup of *HSC-Scl* and *Map17*-based LCH mouse models: tamoxifen was applied for Cre recombination, and mice were then terminally analyzed after 8–16 weeks as indicated.

(B) Representative spectral cytometry pseudocolor and histogram plots of brain myeloid cells enriched using CD45+ beads with microglia (MG), CD206+ border-associated macrophages (BAMs) and CD11a+ macrophages from *BRAF*V600E^Scl^ mice and *BRAF*WT^Scl^ control mice. The abundance of reporter-tagged cells in these populations is displayed in the respective histogram plots.

(C) Correlation between percentage of YFP-tagged cells in the peripheral blood and percentage of YFP-tagged cells in the brains of *BRAF*V600E^Scl^ mice and *BRAF*WT^Scl^ control mice (n = 7–10 mice per group, one experiment).

(D) Experimental setup to generate *BRAF*V600E^Scl^ chimera and *BRAF*WT^Scl^ control chimera.

(E) Statistical analysis of CD11a+ macrophages and percentage of YFP-expressing cells in Microglia, CD206+ BAMs, and CD11a+ macrophages of *BRAF*V600E^Scl^ chimera

and *BRAF*WT^{Scl} control chimera (n = 5 mice per group, two independent experiments, Student's t test).

(F) Expression of key lineage markers in the different brain myeloid cell populations of *BRAF*V600E^{Scl} chimera and *BRAF*WT^{Scl} control chimera (n = 3 per group, two independent experiments).

(G) Experimental setup of intravascular cell staining to determine vascular versus parenchymal localization of cells: *BRAF*V600E^{Scl} mice were injected with a BV510-conjugated anti-CD45 antibody and were shortly after terminally analyzed.

(H) Representative spectral cytometry pseudocolor plots of intravenous CD45 staining for each myeloid cell population (n = 4 mice per group, two independent experiments). See also Figure S1.
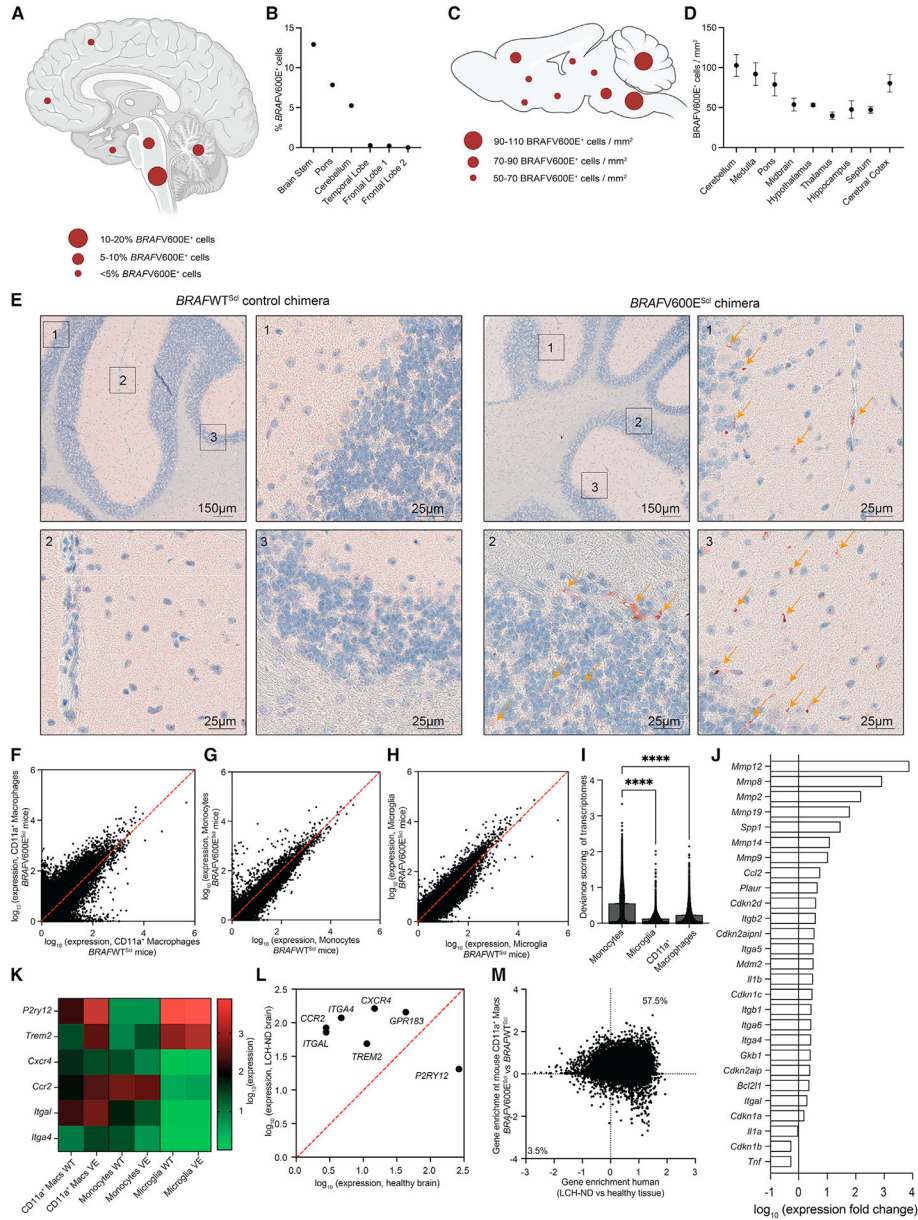
Figure 2. LCH mice with brain-infiltrating *BRAF*V600E-mutated cells share phenotypic and transcriptional characteristics with human LCH-ND

(A) Manifestation of LCH-ND in a schematic human brain (created with biorender.com) and (B) Quantification of *BRAF*V600E transcripts from this specimen. (C) Visualization of the extent to which mouse brains are affected by infiltration with *BRAF*V600E-mutated cells (created with biorender.com) based on the quantification from different brain regions depicted in (D) (n = 4 mice, two independent experiments).

(E) Representative IHC images from the brain of a *BRAF*WT^Scl chimera on the left and *BRAF*V600E^Scl chimera on the right stained for YFP-tagged, BM-derived cells marked with yellow arrows. In *BRAF*WT^Scl chimera, these cells are lineage-traced unmutated cells (left), and in *BRAF*V600E^Scl chimera, these stained cells are *BRAF*V600E^+ cells (right). Scale bar, 150 μm in overview images and 25 μm in enlarged sections.

(F–K) CD11a$^+$ macrophages (F), peripheral blood monocytes (G), and microglia (H) from *BRAF*WT^{Scl} and *BRAF*V600E^{Scl} mice were subjected to bulk RNA sequencing from each 10 mice per group (pooled, one experiment). Gene expression profiles of CD11a$^+$ macrophages (F), monocytes (G), and microglia (H) from *BRAF*WT^{Scl} mice were compared with those from *BRAF*V600E^{Scl} mice in (I) by analysis of the deviance of transcriptomes showing that the transcriptomic remodeling was strongest in CD11a$^+$ macrophages. While monocytes and CD11a$^+$ macrophages in *BRAF*V600E^{Scl} mice are *BRAF*V600E mutated, microglia are unmutated in *BRAF*V600E^{Scl} mice.

(J) The transcriptional remodeling in CD11a$^+$ macrophages was driven by senescence-associated genes, matrix metalloproteinases, and integrins. (K) Comparative analysis of gene expression of key lineage markers in mouse CD11a$^+$ macrophages, peripheral blood monocytes, and microglia.

(L) Comparison of these lineage markers between a human bulk RNA sequencing dataset from an LCH-ND case and human myeloid cells from a healthy brain demonstrating an enrichment for CD11a$^+$ macrophage-defining *Itgal* (encoding integrin alpha L chain, CD11a) as well as *Itga4* (encoding integrin alpha 4 chain, CD49d).

(M) Cross-species comparison of mouse *BRAF*V600E$^+$ CD11a$^+$ macrophages and human LCH-ND material showing that 57.5% of the genes were enriched in mouse and human LCH material.

Data in (D) are shown as means ± s.e.m, ****p < 0.0001. LCH-ND, neurodegenerative LCH; WT, wild type; VE, *BRAF*V600E. See also Figure S2.
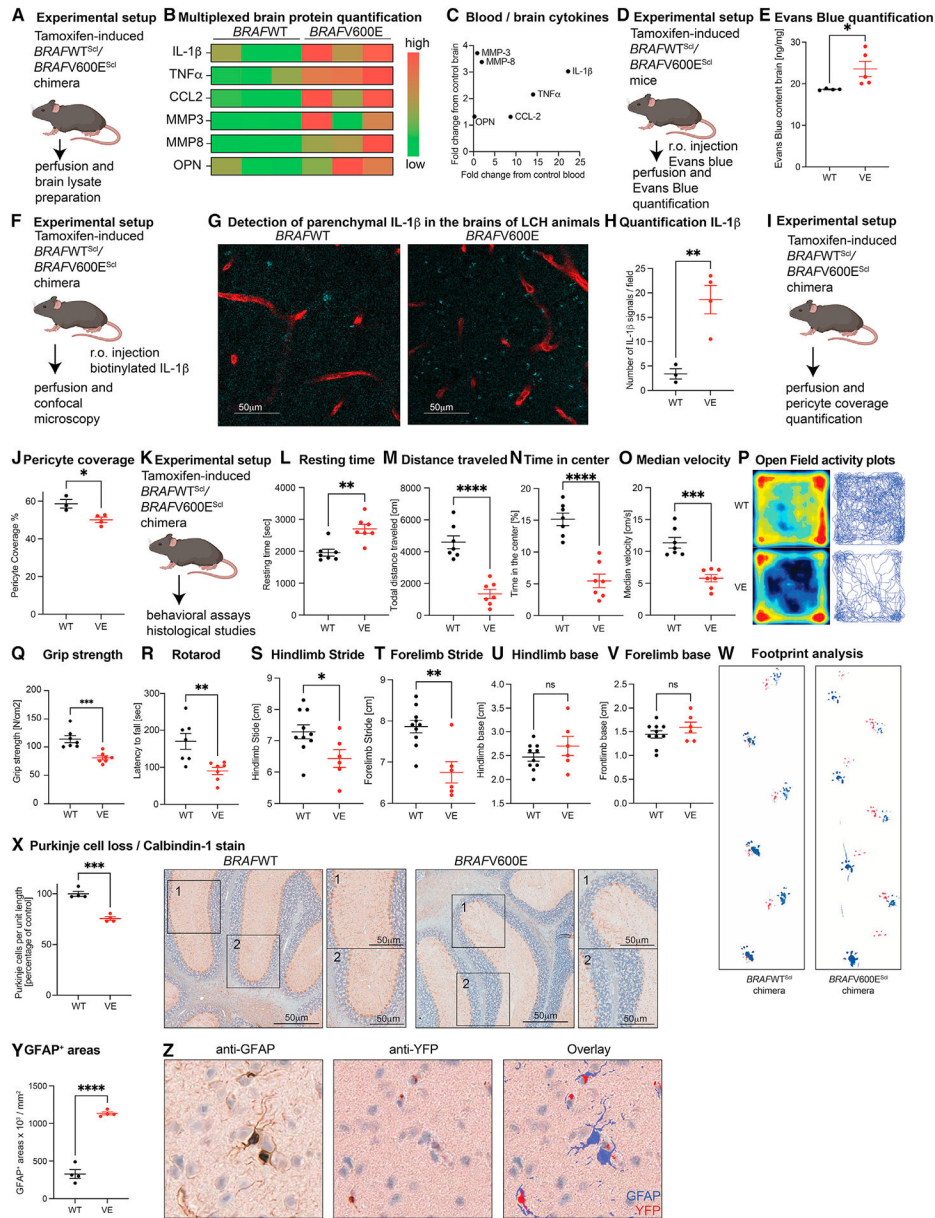
Figure 3. *BRAF*V600E^Scl chimera have a compromised BBB and exhibit behavioral and neurologic abnormalities

(A) Experimental setup to quantify inflammatory cytokines from brain lysates from *BRAF*V600E^Scl and *BRAF*WT^Scl mice.

(B) Multiplexed cytokine detection in the brains of *BRAF*V600E^Scl and *BRAF*WT^Scl control mice (n = 3–4 mice per group, one experiment).

(C) From the multiplex protein dataset, a comparison between the fold change of cytokine concentration between WT and VE in the blood (x axis) and the brain (y axis).

(D) Experimental setup of an Evans Blue-based assay to quantify the permeability of the BBB for small molecules.

(E) Evans Blue experiment demonstrates increased permeability of BBB in BRAFV600Escl mice (n = 4–5 mice per group, two independent experiments).

(F) Experimental setup to assess and quantify the transition of biotinylated IL-1β into the brain of *BRAF*V600E^{Scl} mice and *BRAF*WT^{Scl} control mice.

(G) Representative images of IL-1β (cyan) and Collagen IV (red) showing a scattered perivascular signal derived from biotinylated IL-1β that can be detected in *BRAF*V600E^{Scl} mice but not *BRAF*WT^{Scl} control mice (n = 3–4 mice per group, two independent experiments). Scale bar, 50 μm.

(H) Quantification of IL-1β-derived fluorescent signal shows a significant increase in extravasation of biotinylated IL-1β into the brain parenchyma in *BRAF*V600E^{Scl} mice compared to *BRAF*WT^{Scl} mice (n = 3–4 mice per group, two independent experiments, Student's t test).

(I) Experimental setup to assess the pericyte coverage of brain vessels from *BRAF*V600E^{Scl} and *BRAF*WT^{Scl} chimera.

(J) *BRAF*V600E^{Scl} chimera have a decreased blood vessel coverage with pericytes compared to *BRAF*WT^{Scl} chimera (n = 3–4 mice per group, two independent experiments, Student's t test).

(K) Experimental setup for behavioral assays and histological studies for (L)–(Z).

(L–P) Performance of *BRAF*V600E^{Scl} chimera (VE) and *BRAF*WT^{Scl} chimera (WT) in an open field setup showing a deteriorated performance with reduced resting time (L), distance traveled (M), time in center (N), and median velocity (O) summarized in the activity plots (P) (n = 7 mice per group, two independent experiments, Student's t test).

(Q and R) Grip strength (Q) and latency to fall (R) quantification of *BRAF*V600E^{Scl} and *BRAF*WT^{Scl} chimera in a Rotarod assay (n = 7 mice per group, two independent experiments, Student's t test).

(S–W) Footprint analysis of hindlimb and forelimb stride (S and T, respectively) as well as hindlimb and forelimb base as signs of a motor deficit in *BRAF*V600E^{Scl} chimera (U and V, respectively; n = 6–10 mice per group, pooled from two independent experiments). (W) Representative case of unilateral paralysis in a *BRAF*V600E^{Scl} chimeric mouse compared to a *BRAF*WT^{Scl} mouse; hind paws painted with blue ink and front paws painted with red ink.

(X) Quantification of Purkinje cells in *BRAF*V600E^{Scl} chimera and *BRAF*WT^{Scl} chimera (n = 4 mice per group, two independent experiments, Student's t test) and representative images of Calbindin-1 staining of mouse cerebella, scale bar, 50 μm in overview images and in enlarged sections.

(Y) Quantification of GFAP$^+$ brain regions of multiplex immunohistochemistry of the brains of *BRAF*V600E^{Scl} chimera (n = 4 mice per group, two independent experiments, Student's t test).

(Z) Representative images of multiplex immunohistochemistry of brains of *BRAF*V600E^{Scl} chimera staining for activated astrocytes (anti-GFAP, left), *BRAF*V600E-mutated cells (anti-YFP, middle), and showing co-localization (overlay, right). Student's t test was used with *p < 0.05, **p < 0.01, ***p < 0.001, ****p < 0.0001, n.s., not significant. Data are shown as means ± s.e.m. r.o., retro orbital; GFAP, glial fibrillary acidic protein. See also Figure S3.
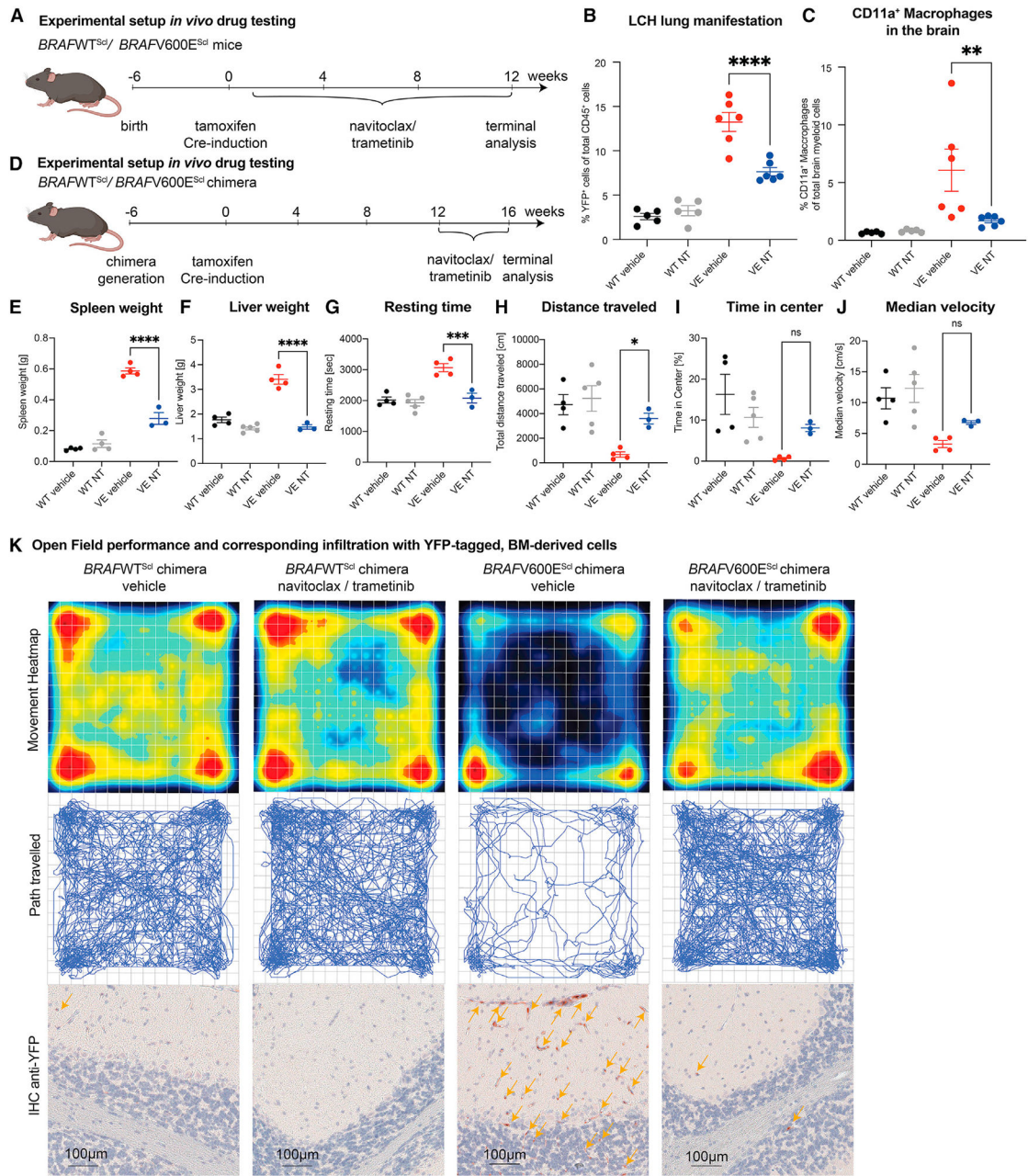
Figure 4. Accumulation of circulating, *BRAF*V600E⁺ cells is a driver of LCH-like disease and combined preventive senolytic/MAPK inhibitor therapy alleviates the disease burden

(A) Experimental setup for preventive *in vivo* drug treatment of *BRAF*WT^Scl mice and *BRAF*V600E^Scl mice with navitoclax/trametinib (NT) or vehicle control.

(B) Percentage of YFP⁺ cells in the lungs of *BRAF*WT^Scl (WT) and *BRAF*V600E^Scl (VE) mice receiving vehicle or NT treatment analyzed by spectral cytometry (n = 5–6 per group, two independent experiments, ANOVA).

(C) Percentage of CD11a⁺ macrophages in the brains of *BRAF*WT^Scl (WT) and *BRAF*V600E^Scl (VE) mice receiving vehicle or NT combination treatment (n = 5–6 per group, two independent experiments, ANOVA).

(D) Experimental setup for *in vivo* drug treatment of *BRAF*WT^{Scl} chimera and *BRAF*V600E^{Scl} chimera with NT or vehicle control.

(E and F) Quantification of the weight of the spleens (E) and the livers (F) of *BRAF*WT^{Scl} (WT) and *BRAF*V600E^{Scl} (VE) chimera receiving vehicle or NT treatment (n = 3–4 mice per group, two independent experiments, ANOVA).

(G–J) Open Field assessment of vehicle- or NT-treated *BRAF*WT^{Scl} (WT) and *BRAF*V600E^{Scl} (VE) chimera with quantification of the resting time (G), distance traveled (H), time in the center (I) and mouse median velocity (J).

(K) Movement heatmap (top row) and path traveled (middle row) in the Open Field assessment with paired anti-YFP IHC from cerebellar regions (bottom row, scale bar, 100 μm) of the respective mice. ANOVA with post-hoc analysis was used with $*p < 0.05$, $**p < 0.01$, $***p < 0.001$, $****p < 0.0001$, n.s., not significant. Data are shown as means ± s.e.m. NT, navitoclax/trametinib; IHC, immunohistochemistry. See also Figure S3.

KEY RESOURCES TABLE

REAGENT or RESOURCE	SOURCE	IDENTIFIER
Antibodies		
rat anti-mouse CD4, clone GK1.5, BV750	BioLegend	Cat#100467; RRID: AB_2734150
rat anti-mouse/human CD11b, clone M1/70, PE-Cy5	BioLegend	Cat#101209; RRID: AB_312793
rat anti-mouse CD45, clone 30-F11, Alexa Fluor 700	BioLegend	Cat#103127; RRID: AB_493715
rat anti-mouse CD45, clone 30-F11, BV510	BioLegend	Cat#103137; RRID: AB_2563061
mouse anti-mouse CD45.1, clone A20, PE	BioLegend	Cat#110707; RRID: AB_313497
rat anti-mouse MHCII, clone M5/114.15.2, BV711	BioLegend	Cat#107643; RRID: AB_2565976
rat anti-mouse Ly-6C, clone HK1.4, BV785	BioLegend	Cat#128041; RRID: AB_2565852
mouse anti-mouse CD8a, clone QA17A07, BV421	BioLegend	Cat#155010; RRID: AB_2814057
rat anti-mouse Ly-6G, clone 1A8, BUV805	BD Biosciences	Cat#741994; RRID: AB_2871294
rat anti-mouse B220, clone RA3-6B2, BV570	BioLegend	Cat#103237; RRID: AB_10900264
rat anti-mouse CD11a, clone M17/4, PerCP/Cy5.5	BioLegend	Cat#101123; RRID: AB_2562932
rat anti-mouse CD206, clone C068C2, PE/Cy7	BioLegend	Cat#141720; RRID: AB_2562248
rat anti-mouse F4/80, clone BM8, eFluor450	Thermo Fisher Scientific	Cat#48-4801-82; RRID: AB_1548747
rat anti-mouse F4/80, clone BM8, APC/Fire750	BioLegend	Cat#123151; RRID: AB_2616725
rat anti-mouse P2RY12, clone S16007D, APC	BioLegend	Cat#848006; RRID: AB_2721468
rat anti-mouse Lyve-1, clone ALY7, eFluor450	Thermo Fisher Scientific	Cat#48-0443-82
rat anti-mouse CD169, clone 3D6.112, BV605	BioLegend	Cat#142413; RRID: AB_2564030
mouse anti-mouse Calbindin-1, polyclonal, pH 9 at 1h RT	Proteintech	Cat#14479-1; RRID: AB_2228318
monoclonal mouse anti-GFP, cross-reactive to YFP, clone JL8, pH9 a 1:200 at 1:200 at 4°C o/n	Takara Bio	Cat#632381; RRID: AB_2313808
polyclonal rabbit anti-DsRed, cross-reactive to tdTomato, pH 9 at 1h RT	Takara Bio	Cat#632496; RRID: AB_10013483
polyclonal rabbit anti-mouse/human GFAP, pH 9 at 1h RT	Agilent Technologies	Cat#Z033429-2
polyclonal rabbit anti-mouse/human MBP, pH6 at 4°C o/n	Thermo Fisher Scientific	Cat#PA5-78397; RRID: AB_2736178
polyclonal goat anti-mouse Aminopeptidase N/CD13, 1:100, 48h	R&D Systems	Cat#AF2335; RRID: AB_2227288
polyclonal rabbit anti-mouse Collagen IV, 1:300, 48h	Bio-Rad	Cat#2150-1470; RRID: AB_2082660
polyclonal goat anti-mouse Podocalyxin, 1:100, 48h	R&D Systems	Cat#AF1556; RRID: AB_354858
polyclonal rabbit anti-RFP/tdTomato, 1:1000	Rockland Immunochemicals	Cat#600-401-379; RRID: AB_2209751
polyclonal AffiniPure donkey anti-goat, Cy5, 1:300-1:400, 24h	Jackson ImmunoResearch Labs	Cat#705-175-147; RRID: AB_2340415
polyclonal AffiniPure donkey anti-rabbit, DyLight488, 1:300-1:400, 24h	Jackson ImmunoResearch Labs	Cat#711-485-152; RRID: AB_2492289
polyclonal donkey anti-rabbit, Alexa Fluor 647, 1:1,000	Thermo Fisher Scientific	Cat#A-31573; RRID: AB_2536183
Biological samples		
Brain autopsy samples for IHC	McClain KL et al.[17], Cancer 2018, PMID: 29624648	N/A
Chemicals, peptides, and recombinant proteins		
Navitoclax	APExBIO	Cat#A3007
Trametinib	Selleck Chemicals	Cat#S2673
Evans Blue	Millipore Sigma	Cat#E2129
Tamoxifen	Millipore Sigma	Cat#T5648-5G

REAGENT or RESOURCE	SOURCE	IDENTIFIER
Avidin, NeutAvidin™, Oregon Green™ 488 conjugate	Thermo Fisher Scientific	Cat#A6374
Super Bright Complete Staining Buffer	Thermo Fisher Scientific	Cat#SB-4401-75
ProcartaPlex™ Cell Lysis Buffer	Thermo Fisher Scientific	Cat#EPX-99999-000
Halt™ Protease Inhibitor Cocktail	Thermo Fisher Scientific	Cat#78430
ProLong™ Gold Antifade Mountant	Thermo Fisher Scientific	Cat#P36930
Recombinant mouse IL-1β	R&D Systems	Cat#201-LB-025/CF
Critical commercial assays		
MILLIPLEX® MAP Mouse Kidney Injury Magnetic Bead Panel 2 - Toxicity Multiplex Assay	Millipore Sigma	Cat#MKI2MAG-94K
MILLIPLEX® MAP Mouse MMP Magnetic Bead Panel 1	Millipore Sigma	Cat#MMMP1MAG-79K
MILLIPLEX® MAP Mouse High Sensitivity T cell Panel-Premix Bulk (Space Saver) Packaging - Immunology Multiplex Assay	Millipore Sigma	Cat#MHSTCMAG-70KPXBK
MILLIPLEX® MAP Mouse MMP Magnetic Bead Panel 2 - Immunology Multiplex Assay	Millipore Sigma	Cat#MMMP2MAG-79K
RNeasy Plus Mini	Qiagen	Cat#74034
EZ-Link™ Sulfo-NHS-Biotin kit	Thermo Fisher Scientific	Cat#A39256
LIVE/DEAD™ Fixable Blue Dead Cell Stain Kit, for UV excitation	Thermo Fisher Scientific	Cat#L23105
Deposited data		
RNA sequencing from human purified CNS cell types	Zhang et al.[30]	GEO: GSE73721
Bulk RNA sequencing from histiocytic neoplasms	Diamond et al.[18]	GEO: GSE74442
Bulk RNA sequencing from LCH-mouse brain myeloid cell fractions	This paper	GEO: GSE227984
Experimental models: Organisms/strains		
Mouse: C57BL/6-Tg(Tal1-cre/ERT)42-056Jrg/J (HSC-SCL-CreER)	The Jackson Laboratory	RRID: IMSR_JAX:037466
Mouse: 6.129X1-*Gt(ROSA)26Sor^tm1(EYFP)Cos*/J (YFP)	The Jackson Laboratory	RRID: IMSR_JAX:006148
Mouse: 6.Cg-*Gt(ROSA)26Sor^tm14(CAG-tdTomato)Hze*/J (tdTomato)	The Jackson Laboratory	RRID: IMSR_JAX:007914
Mouse: B6.SJL-*Ptprc^aPepc^b*/BoyJ (CD45.1)	The Jackson Laboratory	RRID: IMSR_JAX:002014
Mouse: B6.129P2(Cg)-Braftm1Mmcm/J	The Jackson Laboratory	RRID: IMSR_JAX:017837
Mouse: Pdzk1ip1-CreER (*MAP17-CreER*)	Sawai et al.[15], Immunity 2016, PMID: 27590115	N/A
Software and algorithms		
ImageJ	Schneider et al.	https://ImageJ.nih.gov/ij/
QuPath v0.3.2	Bankhead P et al.	https://qupath.readthedocs.io
FlowJo Version 10	Becton Dickinson	N/A
SpectroFlo v2.2.0.3	Cytek Biosciences	N/A
Fusion 5.6	Omnitech Electronics	N/A
Prism 10	GraphPad by Dotmatics	N/A
BioRender Ullustration design tool	BioRender	https://biorender.com
Adobe Illustrator 2024	Adobe	
R	R Development Core Team, 2008 *edgeR, limma, EnhancedVolcano,*	http://www.R-project.org

REAGENT or RESOURCE	SOURCE	IDENTIFIER
	clusterProfiler, enrichplot, ggplot2, ggridges, pathview	